

Identification of Low-Level Point Radiation Sources Using a Sensor Network

Nageswara S. V. Rao, Mallikarjun Shankar
Oak Ridge National Laboratory

Jren-Chit Chin, David K. Y. Yau
Purdue University

Srinivasagopalan Srivathsan, S. Sitharama Iyengar
Louisiana State University

Yong Yang, Jennifer C. Hou
University of Illinois at Urban-Champaign

Abstract—Identification of a low-level point radiation source amidst background radiation is achieved by a network of radiation sensors using a two-step approach. Based on measurements from three sensors, the geometric difference triangulation method is used to estimate the location and strength of the source. Then a sequential probability ratio test based on current measurements and estimated parameters is employed to finally decide: (1) the presence of a source with the estimated parameters, or (2) the absence of the source, or (3) the insufficiency of measurements to make a decision. This method achieves specified levels of false alarm and missed detection probabilities, while ensuring a close-to-minimal number of measurements for reaching a decision. This method minimizes the ghost-source problem of current estimation methods, and achieves a lower false alarm rate compared with current detection methods. This method is tested and demonstrated using: (1) simulations, and (2) a test-bed that utilizes the scaling properties of point radiation sources to emulate high intensity ones that cannot be easily and safely handled in laboratory experiments.

Index Terms—Point radiation source, detection and localization, sequential probability ratio test.

I. INTRODUCTION

There has been an increasing interest in the identification of *low-level* radiation sources as a part of the defense strategy against dirty bomb scenarios. The ability to identify the signatures of such sources will enable their detection before they are set off, in particular, while they are being transported or stored. Or, in another scenario, we will be able to detect radiation traces and estimate their extent in seemingly conventional explosions, so that first responders can be forewarned and suitably protected against the low-level yet highly hazardous radiation. Typically, in both of these scenarios, the radiation levels may be low enough to appear as “normal” variations of the background radiation. The detection problem is particularly acute since the radiation measurements follow the Poisson process, whose variance is of the same order as the radiation level itself. While long-term averages of measurements due to low-level sources do result in elevated levels which eventually can be

detected, our focus is on identifying the sources quickly to ensure fast response. In general, the area of detecting various radiation sources using individual sensors has been well established in terms of both detection devices and detection methods [14], [18], most of which are dedicated to single or co-located sensor systems. Recent advances in sensor network technologies, however, have opened up the potential for improved detection, as well as the estimation of source parameters, by utilizing measurements from multiple, geographically dispersed sensors; see, for example, [7], [10], [15], [19], [22], [23] for this line of work.

Compared with the identification of high intensity radiation sources, the detection and localization of low-level sources is difficult due to two major factors:

- (A) **Varied background radiation:** The background radiation depends on both local natural and man-made sources and global sources such as cosmic rays, and hence it may vary significantly from one deployment region to another. If not carefully interpreted, such measurements lead to “ghost” sources (false alarms) that may cause unnecessary panic.
- (B) **Probabilistic radiation measurements:** The radiation sources generate inherently probabilistic measurements; typically, gamma radiation from point sources follows the Poisson distribution [14], [16].

The combined effect of these two factors makes it hard to derive *a priori* thresholds needed by traditional detection methods. Furthermore, the estimation of source location parameters cannot be directly solved by the triangulation methods developed for deterministic measurements. On the other hand, the estimation can be made more effective when a network of sensors is employed, provided that a number of remaining estimation problems can be solved. In this paper, we address Factor (A) above by in-situ estimation of background radiation during initial network deployment. We address Factor (B) above using a combined geometric localization method and the sequential probability ratio test (SPRT).

Probability ratio tests are typically employed in the *detection* problems to derive thresholds to achieve specified levels of false alarm rates and missed detection rates, in both centralized [24] and distributed detection systems [25]. Such an approach is described for the detection of radiation sources using single sensors in [9], [12], [18] (to name a few examples) and using copula methods in sensor networks [23]. The estimation of the location and strength of point radiation sources typically requires at least three sensors and is solved using the least square methods in [11], [10], [17]. Typically, the *parameter estimation* methods implicitly assume that the measurements are due to a real source and not just the background, often by utilizing a preceding detection step. For low-level sources, however, it is not as easy to discriminate between source and background measurements, and existing methods often return results corresponding to “ghost” sources.

In this paper, we show that the detection and parameter estimation steps can reinforce each other, in a two-step decision procedure for low-level radiation sources. We present a method for the *identification* – which subsumes the detection and parameter estimation – of a point radiation source using a network of three sensors that provide radiation counts. In the first step, we utilize a geometric localization method to estimate the location of a real or ghost source, from which we also estimate the source strength. Then, using the estimated source parameters, we utilize SPRT to declare: (1) the presence of a source with the estimated parameters, or (2) the absence of the source, or (3) the insufficiency of the collected measurements to make a decision. The localization method is derived by adapting the recently developed geometric difference-triangulation method [21] to our problem, which does not have the numerical vulnerabilities of least squares or linear methods. The source strength is estimated using a linear combination of the estimates from individual sensors. The detection test utilizes the estimated background radiation of the given deployment region and the estimated source parameters, to formulate SPRT based on the Poisson point source model. Ghost sources, if estimated in the first step, will be rejected by the SPRT within a specified false alarm rate, since they do not lead to statistically consistent measurements. On the other hand, the estimated parameters enable us to formulate a more specific SPRT compared with detecting a general increase in the radiation level, which in turn yields a decision with the least expected number of measurements. Our approach is in contrast to conventional approaches in which detection precedes identification as in several tracking applications [6], [5].

Evaluating identification methods for radiation sources

poses pragmatic challenges of experimentation, since it is potentially hazardous and too expensive to deploy and clean-up the effects of radiation sources of all but minimal strengths. We exploit the simple product form of the radiation model to develop a scaled-down workbench that emulates higher-intensity sources and larger-scale deployments. In particular, we map the workbench of a few feet in dimension to emulate deployments of several hundred meters, and demonstrate the effectiveness of our method using real but safe low-level radiation sources.

The balance of the paper is organized as follows. In Section II, we briefly review the related work on the detection and estimation of radiation sources, with an emphasis on sensor network solutions. We formulate the identification problem in Section III. We describe our solution to the source parameter estimation problem in Section IV and the detection problem in Section V. We combine the estimation and detection results to develop our identification method in Section VI. We present our simulation results in Sections IV and VI, and test-bed and emulation results in Section VII.

II. RELATED WORK

The detection and estimation of radiation sources of various kinds has been well studied, particularly using single sensors [14], [4]. The detection of radiation sources amidst background radiation has been studied using SPRT for various scenarios such as long-term and portal monitoring [8], [12], [18]. The existing work using SPRT does not address the source localization problem.

The use of a network of sensors for detecting and tracking radiation sources has been more recently proposed. For the detection of radioactive sources, a linear arrangement of detectors has been considered in [19], [7], [15], and an analysis of sensor network solutions has been carried out for a source moving in a linear path [22]. The detection of a point radiation source using a sensor network is addressed in [23], wherein sensor measurements are combined using a copula function that captures the sensor correlations.

Typically, a detection method is used to first assert the presence of a radiation source, and *then*, measurements from multiple sensors are used to estimate the parameters of the source. The problem of localizing a point radiation source has been addressed in [10], [17], [3]. Recursive and moving horizon non-linear least square methods have been proposed to track radioactive sources in [11]. Overall, the existing estimation methods assume that the measurements correspond to a real source (i.e., the source does exist), whereas the detection methods can be made more effective when the source parameters are accurately known. Our focus in this paper is to jointly address the detection and estimation problems by closely coupling the two decisions.

III. PROBLEM FORMULATION

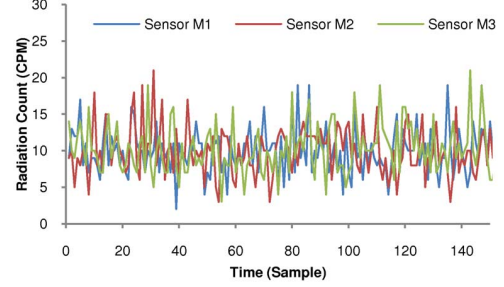
We consider the identification of a point radiation source S of unknown strength A_u expressed as Counts Per Minute (CPM)¹, called the *source rate*, and located at an unknown location (x_u, y_u) . The source gives rise to a radiation intensity of $I(x, y) = A_u/r^2$ at any point (x, y) , where $r = d((x_u, y_u), (x, y)) = \sqrt{(x_u - x)^2 + (y_u - y)^2}$. Let $m_{i,1}, m_{i,2}, \dots, m_{i,n_i}$ be a sequence of radiation counts, each measured per unit time, at the sensor M_i at known location (x_i, y_i) , for $i = 1, 2, 3$. The radiation count due to the source observed at M_i per unit time is a Poisson random variable with parameter $\lambda = I(x_i, y_i)$, not accounting for the background radiation [14], [16].

Let $B(x, y)$ denote the background radiation strength at (x, y) expressed as CPM, called the *background rate*. The radiation count measurement (due to the background radiation) at a sensor i located at (x_i, y_i) is given by the Poisson random variable with parameter $B(x_i, y_i)$. The assumption of Poisson distribution for the background measurements may not always be accurate, since the background radiation may be a complex combination of various sources; we utilize this assumption in our main derivation and later account for possible deviations. On the other hand, measurements of $I(x_i, y_i)$, being from a single point source, are more accurately characterized by the Poisson distribution. In either case, the measurements are statistically independent across the temporal dimension, and exhibit significant variations as shown in Figure 1.

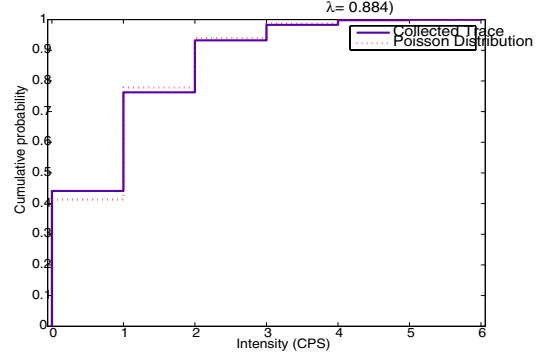
We consider a monitoring area contained within the acute triangle formed by M_1, M_2, M_3 (as shown in Figure 2 for an example) to simplify the presentation of the localization method; the triangle property is not needed in practice, as the presented method can be shown to work for general geometries [21], [27]. We are given three sequences of measurements, from M_i for $i = 1, 2, 3$, collected within the same time window. The *detection problem* is concerned with inferring the presence of a source, whereas the *estimation problem* is concerned with estimating the location (i.e., the localization problem) and the strength of the source, if present. The estimates of (x_u, y_u) and A_u are denoted by (\hat{x}_u, \hat{y}_u) and \hat{A}_u , respectively.

We characterize the solution of the detection problem by the *false alarm probability* $P_{1,0}$, corresponding to the probability of declaring the presence of a source when none exists, and the *missed detection probability* $P_{0,1}$, corresponding to the probability of declaring the presence of only the background radiation when a source is present in the monitoring area. In addition, we

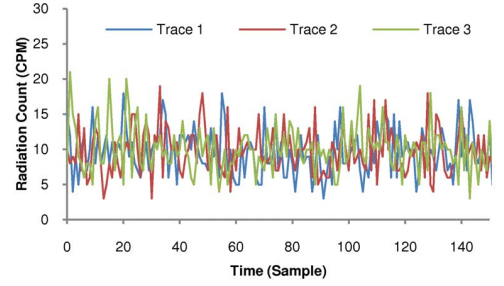
¹Sensor measurements accumulated over different time windows are typically “normalized” and expressed as CPM.



(a) Measurements from RFTrax radiation sensors.



(b) Pdf of RFTrax measurements.



(c) Simulated Poisson variables with $\lambda = 10$.

Fig. 1. Background radiation counts show high variance.

characterize the timeliness of the solution method by the *detection time* which is the size of the time window or the number of measurements needed to declare the presence or absence of a radiation source.

IV. SOURCE PARAMETER ESTIMATION

In this section, we first present a method to estimate (\hat{x}_u, \hat{y}_u) using an extension of the geometric triangulation method in [21]. We then describe a linear fuser to estimate the source strength A_u .

A. Location Estimation

Let $m_{i,1}, m_{i,2}, \dots, m_{i,n_i}$ denote a sequence of n_i measurements collected by the sensor M_i within a given time window. Using the measurements, we compute the mean of measurements at each sensor

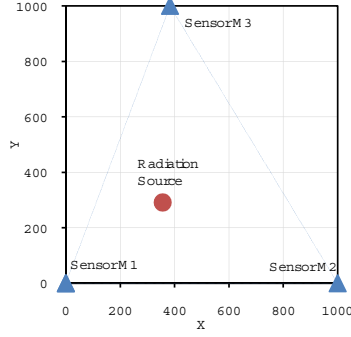


Fig. 2. Region monitored by three sensors forming an acute triangle.

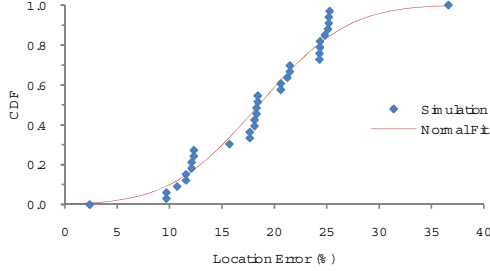


Fig. 3. Errors of location estimation method for 50 simulation runs. The red curve denotes the best fit to normal distribution.

given by $\bar{m}_i = \frac{1}{n_i} \sum_{j=1}^{n_i} m_{i,j}$ for $i = 1, 2, 3$. The mean is an unbiased estimate of A_u/r_i^2 for $r_i = \sqrt{(x_u - x_i)^2 + (y_u - y_i)^2}$. In terms of expectations, we have $\frac{1}{2} \ln(E[\bar{m}_i]/E[\bar{m}_k]) = \ln r_i - \ln r_k$, which is the difference of distances to the sensors M_i and M_k from the source in ln-space. Let $\delta_{i,k} = \frac{1}{2} \ln(\bar{m}_i/\bar{m}_k)$, such that $\delta_{i,k} = \ln r_i - \ln r_k$ is valid on the average. Let $L_{i,k}$ denote the set of all points (x_u, y_u) on a plane such that $\ln r_i - \ln r_k = \delta_{i,k}$ for sensors M_i and M_k with fixed locations. Our localization method is based on binary search on $L_{1,2}$ which uses $\delta_{1,3}$ as an objective function to locate a point (\hat{x}_u, \hat{y}_u) , such that $|x_u - \hat{x}_u| \leq \epsilon$ and $|y_u - \hat{y}_u| \leq \epsilon$. The implementation details of the search algorithm can be found in [?].

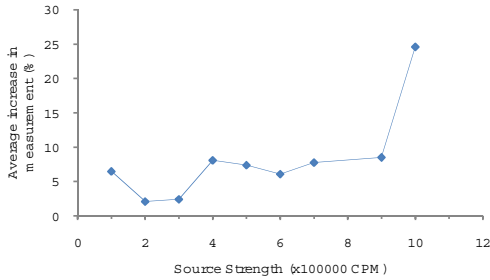


Fig. 4. Percentage increase in radiation level over background level due to sources with $A_u = 2 \times 10^5, 5 \times 10^5, 6 \times 10^5, 7 \times 10^5, 10 \times 10^5$ CPM.

We now establish the correctness of the binary search method by establishing that on $L_{1,2}$ the function $\delta_{1,3}$ varies monotonically so that the binary search can be supported². We show the monotonicity in ln-space for the scenario of Figure 2, and the general case can be proved along the lines of [?]. Without loss of generality, we assume following generic configuration:

- (a) $M_1 = (0, 0)$, $M_2 = (x_2, 0)$ and $M_3 = (x_3, y_3)$ such that $x_2 > 0$, $x_3 > 0$ and $y_3 > 0$. Also, $x_3 < x_2$.
- (b) The source S is located at (x_u, y_u) such that $x_u > 0$ and $y_u > 0$, and S is closer to M_1 than to M_2 and M_3 ; otherwise we can rotate the triangle and re-label the sensors by their coordinates.

We have $d(S, M_i) = r_i = \sqrt{(x_u - x_i)^2 + (y_u - y_i)^2}$, and let $\Delta(M_i, M_j) = \ln[d(S, M_i)] - \ln[d(S, M_j)]$, for $i, j = 1, 2, 3$. Then, we have

$$\frac{\partial d(S, M_i)}{\partial x_u} = \frac{(x_u - x_i)}{d(S, M_i)}$$

and

$$\frac{\partial d(S, M_i)}{\partial y_u} = \frac{(y_u - y_i)}{d(S, M_i)}.$$

By Item (b) we have $d(S, M_1) < d(S, M_2)$ and $d(S, M_1) < d(S, M_3)$.

The directional derivative of $\Delta(M_1, M_3)$ on the locus $\{(x_u, y_u) | \Delta(M_1, M_2) = \delta_{12}\}$, for any δ_{12} , is given by

$$\begin{aligned} & \nabla_{\Delta(M_1, M_2)} \Delta(M_1, M_3) \\ &= \left[\frac{\partial \Delta(M_1, M_2)}{\partial x_u}, \frac{\partial \Delta(M_1, M_2)}{\partial y_u} \right]^T \circ \frac{1}{K} \left[\frac{\partial \Delta(M_1, M_3)}{\partial x_u}, \frac{\partial \Delta(M_1, M_3)}{\partial y_u} \right] \\ &= \left[\frac{x_u}{[d(S, M_1)]^2} - \frac{x_u - x_3}{[d(S, M_3)]^2}, \frac{y_u}{[d(S, M_1)]^2} - \frac{y_u - y_3}{[d(S, M_3)]^2} \right]^T \\ & \quad \circ \frac{1}{K} \left[\frac{x_u}{[d(S, M_1)]^2} - \frac{x_u - x_2}{[d(S, M_2)]^2}, \frac{y_u}{[d(S, M_1)]^2} - \frac{y_u - y_2}{[d(S, M_2)]^2} \right] \\ &= \left(\frac{x_u}{[d(S, M_1)]^2} - \frac{x_u - x_3}{[d(S, M_3)]^2} \right) \left(\frac{x_u}{[d(S, M_1)]^2} - \frac{x_u - x_2}{[d(S, M_2)]^2} \right) \\ & \quad + \left(\frac{y_u}{[d(S, M_1)]^2} - \frac{y_u - y_3}{[d(S, M_3)]^2} \right) \left(\frac{y_u}{[d(S, M_1)]^2} - \frac{y_u - y_2}{[d(S, M_2)]^2} \right) \end{aligned}$$

$$\text{where } K = \left[\left(\frac{\partial \Delta(M_1, M_3)}{\partial x_u} \right)^2 + \left(\frac{\partial \Delta(M_1, M_3)}{\partial y_u} \right)^2 \right]^{-1/2}.$$

Note that $x_2 > 0$, $x_3 > 0$ and $y_3 > 0$. Also $d(S, M_3) > d(S, M_1)$ and $d(S, M_2) > d(S, M_1)$. Then, we conclude that $\nabla_{\Delta(M_1, M_2)} \Delta(M_1, M_3) > 0$, for all $x_u > 0$ and $y_u > 0$.

We now present simulation results to illustrate the performance of the above method. The simulation programs are implemented in C using random number generators

²The monotonicity proof of [?] is valid for $\delta_{i,k} = r_i - r_k$ in the distance space as opposed to the ln-space here.

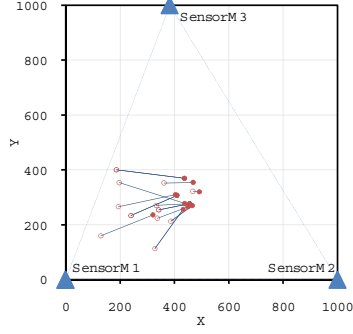


Fig. 5. Examples of actual source locations (red color filled circles) and their estimators (non-filled circles) joined by line segments.

from Numerical Recipes [20] and executed on a Redhat Linux workstation with a 2.8 GHz Intel processor. Using 1000 randomly generated source locations with strength³ $A_u = 10^6$ CPM and $B = 10$ CPM, the errors in the location estimation as a percentage of the distance between the sensors are shown in Figure 3. The average error is 20.07% for 1000 randomly located sources but the errors have a high variance due to the Poisson measurements; the x-coordinate of the top sensor (M_3) is randomly chosen from $[1, 1000]$ m while the y-coordinate is fixed at 1000m. Some example source locations and their estimators are shown in Figure 5, wherein a line segment joins the actual location of the source (shown as red color filled circles) with its estimator (shown as non-filled circles).

We executed this location estimation algorithm when there is no source (i.e., there are background measurements only) with $B = 10$ and 100 CPM at the sensors. As shown in Figure 6, the ghost sources have been identified approximately near the centroid of the triangle formed by the sensors when measurements are repeated. In the next section, we outline a method that utilizes the estimated source parameters in SPRT to rule out such ghost sources at a specified rate.

B. Source Strength Estimation

Using the source location estimate (\hat{x}_u, \hat{y}_u) , we have three source strength estimates A_u given by $\hat{A}_i = \bar{m}_i \hat{r}_i^2$, for $i = 1, 2, 3$, where $\hat{r}_i = \sqrt{(x_i - \hat{x}_u)^2 + (y_i - \hat{y}_u)^2}$. We combine these three estimators using coefficients that are inversely proportional to their variance estimates. Since for the Poisson process, both the mean and variance are given by its parameter \bar{m}_i , more weight is given to estimates with a lower variance. Thus, we have the

³The source strengths in the range $[10^5, 10^6]$ CPM are still low-level, despite their apparently large absolute magnitude, since they generate only small increases (less than 20%) in the measurements over a $1000\text{m} \times 1000\text{m}$ monitoring area as shown in Figure 4, due to the quadratic decay of the intensity with respect to distance.

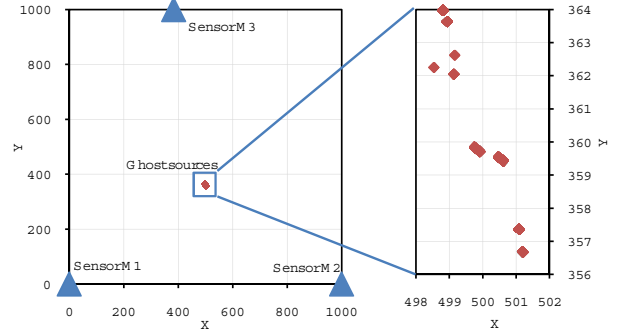


Fig. 6. Estimated location of ghost sources under repeated measurements with an expanded view on the right.

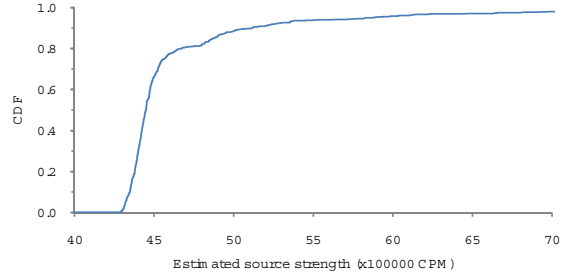


Fig. 7. Variation of source strength estimator for $A_u = 5 \times 10^5$ CPM.

following fused source strength estimator

$$\hat{A}_u = \sum_{i=1}^3 \hat{a}_i \hat{A}_i$$

where $\hat{a}_i = \frac{1/\bar{m}_i}{\sum_{k=1}^3 1/\bar{m}_k}$. The signal strength estimates for 1000 simulated sources with $A_u = 5 \times 10^5$ CPM and $B = 10$ CPM are shown in Figure 7, which show significant variations. The average values of the fused source term estimator for source strength in the range $[5 \times 10^5, 10^6]$ CPM are shown in Figure 8.

V. SOURCE DETECTION

In this section, we describe an SPRT for detecting the presence of a source of estimated rate \hat{A}_u against the estimated background rate of \hat{B}_i at sensor M_i .

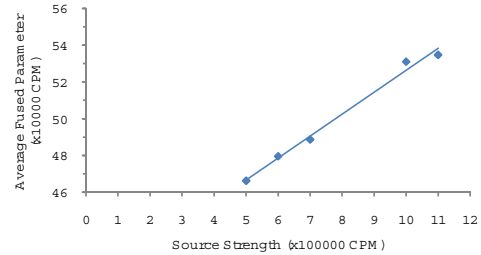


Fig. 8. Average fused source strength estimator.

A. SPRT Test

Consider the measurements $m_{i,1}, m_{i,2}, \dots, m_{i,n_i}$ collected by sensor M_i within a given time window and the estimate of background radiation \hat{B}_i at this sensor location. By the definition of the Poisson process, we have

$$P(m_{i,j}) = \frac{C^{m_{i,j}} e^{-C}}{m_{i,j}!}$$

with parameter C . We utilize the estimate $C = \hat{A}_u/\hat{r}_i^2 + \hat{B}_i$ if the source is present; and $C = \hat{B}_i$ if the source is not present. Let H_C , for $C \in \{\hat{A}_u/\hat{r}_i^2 + \hat{B}_i, \hat{B}_i\}$, denote the hypothesis that the measurements correspond to the intensity level C at the sensor M_i . Now consider the likelihood function

$$l(m_{i,1}, m_{i,2}, \dots, m_{i,n_i} | H_C) = \prod_{j=1}^{n_i} \frac{C^{m_{i,j}} e^{-C}}{m_{i,j}!}$$

wherein we utilize the statistical independence property of the measurements. We now consider the following SPRT based on sensor measurements at M_i .

$$L_{\hat{A}_u/\hat{r}_i^2, \hat{B}_i; n_i} = \frac{l(m_{i,1}, m_{i,2}, \dots, m_{i,n_i} | H_{\hat{A}_u/\hat{r}_i^2 + \hat{B}_i})}{l(m_{i,1}, m_{i,2}, \dots, m_{i,n_i} | H_{\hat{B}_i})}$$

Then, we utilize SPRT [13] as follows:

- (i) If $L_{\hat{A}_u/\hat{r}_i^2, \hat{B}_i; n_i} < \frac{P_{0,1}}{1-P_{1,0}}$, then declare the background, namely $H_{\hat{B}_i}$;
- (ii) Else if $L_{\hat{A}_u/\hat{r}_i^2, \hat{B}_i; n_i} > \frac{1-P_{0,1}}{P_{1,0}}$, then declare that a source with intensity \hat{A}_u is present at location (\hat{x}_u, \hat{y}_u) , namely $H_{\hat{A}_u/\hat{r}_i^2 + \hat{B}_i}$;
- (iii) Otherwise, declare that the measurements are not sufficient to make a decision and continue collecting additional measurements.

The following are the important properties of the SPRT [13]:

- (a) The expected false alarm and miss detection rates of SPRT are given by $P_{1,0}$ and $P_{0,1}$, respectively.
- (b) Among all tests to decide between $H_{\hat{A}_u/\hat{r}_i^2 + \hat{B}_i}$ and $H_{\hat{B}_i}$ with the given $P_{1,0}$ and $P_{0,1}$, SPRT minimizes $E[n_i | H_{\hat{B}_i}]$ and $E[n_i | H_{\hat{A}_u/\hat{r}_i^2 + \hat{B}_i}]$ (see Theorem 2.4, [26], for example).

This test can be compactly expressed as

$$\frac{P_{0,1}}{1-P_{1,0}} \leq L_{\hat{A}_u/\hat{r}_i^2, \hat{B}_i; n_i} \leq \frac{1-P_{0,1}}{P_{1,0}}$$

which can also be expressed in terms of the mean of measurements:

$$\frac{\ln\left[\frac{P_{0,1}}{1-P_{1,0}}\right] + n_i \hat{A}_u/\hat{r}_i^2}{\ln\left[\frac{\hat{A}_u/\hat{r}_i^2 + \hat{B}_i}{\hat{B}_i}\right]} \leq \sum_{j=1}^{n_i} m_{i,j} \leq \frac{\ln\left[\frac{1-P_{0,1}}{P_{1,0}}\right] + n_i \hat{A}_u/\hat{r}_i^2}{\ln\left[\frac{\hat{A}_u/\hat{r}_i^2 + \hat{B}_i}{\hat{B}_i}\right]} \quad (1)$$

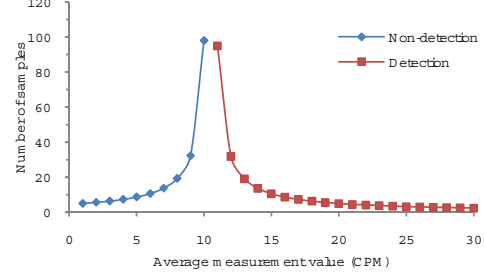


Fig. 9. Number of samples for SPRT to make a conclusion at sensor M_i for $A_u/r_i^2 = 1$ CPM, $B_i = 10$ CPM, $P_{0,1} = 0.01$, $P_{1,0} = 0.01$.

Notice that the bounds on the measurement sum $\sum_{j=1}^n m_{i,j}$ increase linearly with the number of measurements.

The above SPRT is derived under the assumption that the measurements corresponding to both background and source radiation satisfy the Poisson distribution. While point radiation sources follow such a distribution, it may not be the case for background radiation of a more complex nature, primarily because the background radiation could be a combination of multiple sources. In such a case, the false alarm rate of our SPRT method can be different, and can be approximated by the area under the background rate distribution $P_B(x)$ for $x \leq \ln \frac{1-P_{0,1}}{P_{1,0}} + n \frac{\hat{A}_u/\hat{r}_i^2}{\ln((\hat{A}_u/\hat{r}_i^2 + \hat{B}_i)/\hat{B}_i)}$. This distribution can be estimated by utilizing the empirical distribution of the background radiation at the sensor location as described in Section VIIC.

B. Sample Size Estimates

Dividing both sides of Equation (1) by n_i yields

$$\bar{m}_i = \frac{\sum_{j=1}^n m_{i,j}}{n_i} > \frac{\ln\left(\frac{1-P_{0,1}}{P_{1,0}}\right) + n_i \cdot \hat{A}_u/\hat{r}_i^2}{n_i \ln \frac{\hat{A}_u/\hat{r}_i^2 + \hat{B}_i}{\hat{B}_i}}$$

Solving the above equation for the critical value of n_i such that the above inequality holds, we have

$$n_i = \frac{\ln\left(\frac{1-P_{0,1}}{P_{1,0}}\right)}{\bar{m}_i \ln \frac{\hat{A}_u/\hat{r}_i^2 + \hat{B}_i}{\hat{B}_i} - \hat{A}_u/\hat{r}_i^2} \quad (1)$$

The number of measurements required for SPRT to conclude $H_{\hat{A}_u/\hat{r}_i^2 + \hat{B}_i}$ is given by Equation 1 if n_i evaluates to a positive value. A non-positive value of n_i denotes that SPRT will never conclude $H_{\hat{A}_u/\hat{r}_i^2 + \hat{B}_i}$. Similarly, the number of measurements required for SPRT to conclude $H_{\hat{B}_i}$ is given by

$$n_i = \frac{\ln\left(\frac{P_{0,1}}{1-P_{1,0}}\right)}{\bar{m}_i \ln \frac{\hat{A}_u/\hat{r}_i^2 + \hat{B}_i}{\hat{B}_i} - \hat{A}_u/\hat{r}_i^2}$$

Because \hat{B}_i and \hat{A}_u/\hat{r}_i^2 are estimated, errors in the estimation may cause an undesirably long detection time. Furthermore, variance of \bar{m}_i is relatively large because it is averaged over a small number of samples. We quantify the number of measurements required in the presence of non-perfect estimation and measurements. Figure 9 shows the number of measurements required for SPRT to conclude either $H_{\hat{A}_u/\hat{r}_i^2 + \hat{B}_i}$ or $H_{\hat{B}_i}$ for a source measurement that is only 10% higher than the background, and false alarm and miss detection rates both equal to 1%. The figure shows that even with a low dose radiation source, SPRT can make a conclusion using 97 samples on average, in the worst case. This corresponds to 6 minutes of measurements using an RFTrax radiation sensor with a 4 second sampling interval.

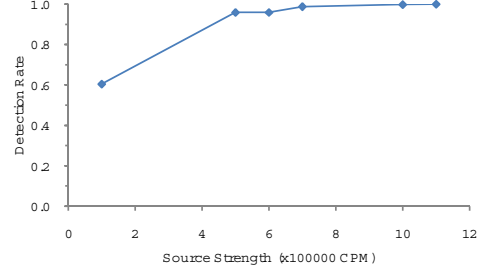
VI. IDENTIFICATION METHOD

We now combine the source parameter estimation and SPRT methods in the previous sections to develop a method for source identification. Initially, the system is put into training mode where the background radiation measurements are collected by each sensor and averaged to estimate the local background radiation level \hat{B}_i . Then, the network is put into monitoring mode, and the identification of the source is achieved using the following procedure:

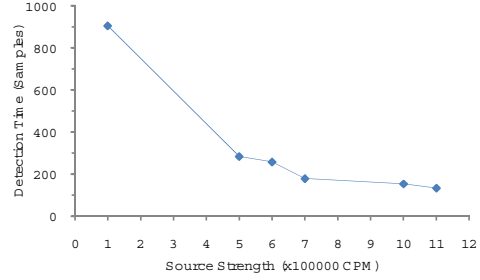
- (i) Using the readings from three sensors, we estimate the source location (\hat{x}_u, \hat{y}_u) and compute the source intensity estimate \hat{A}_u .
- (ii) We utilize SPRT $L_{\hat{A}_u/\hat{r}_i^2, \hat{B}_i; n_i}$ to conclude $H_{\hat{A}_u/\hat{r}_i^2 + \hat{B}_i}$ versus $H_{\hat{B}_i}$ at sensor M_i . We declare $H_{\hat{A}_u/\hat{r}_i^2 + \hat{B}_i}$ or $H_{\hat{B}_i}$ if and only if the respective threshold conditions are satisfied at two or three of the sensors M_i , $i = 1, 2, 3$. Otherwise, more measurements will be collected.

Initially, the default hypothesis is $H_{\hat{B}_i}$, and the hypothesis will be changed only if $H_{\hat{A}_u/\hat{r}_i^2 + \hat{B}_i}$ is declared by a majority of sensors.

The above procedure has the minimum false alarm rate of the two or three sensors that declare $H_{\hat{A}_u/\hat{r}_i^2 + \hat{B}_i}$ to assert the presence of a source. The method was tested using 1000 randomly generated sources with $A_u = 10^5, 5 \times 10^5, 6 \times 10^5, 7^5, 10 \times 10^5$ CPM. The average increase in the radiation level over the background at these source strengths is below 10% for most of the cases, as shown in Figure 4. However, over a short time period, variations due to the background could reach 100%. The detection rates for various source strengths are shown in Figure 10(a) for $P_{0,1} = P_{1,0} = 0.1$, which is 100% for $A_u = 10^6$ CPM or higher. Note that the detection rate is higher than 95% for $A_u = 4 \times 10^5$ CPM or higher even though the average increase in the radiation level at the sensor locations is within the range of [5, 10] percent.



(a) Average detection rate.



(b) Average detection time.

Fig. 10. Performance of the proposed identification method.

The detection times are shown in Figure 10(b), which show a decreasing trend with increasing A_u . Such trend is expected since it is easier in general to detect sources of higher strengths. The average detection time is less than 300 samples (or measurements) for $A_u = 4 \times 10^5$ CPM or higher, even though the average increase in the radiation level at the sensor locations is within [5, 10] percent. However, the actual detection times show significant variations as shown in Figure 11(a), for the case of $A_u = 10^6$ CPM.

When no source is present, the ghost source will be likely located at the centroid of the triangle formed by the sensors. In this case, however, the corresponding high threshold for $H_{\hat{A}_u/\hat{r}_i^2 + \hat{B}_i}$ in Step (ii) will not be met and hence, the false alarm will be cleared. In our simulations with 10000 measurements with $B = 10, 100$ CPM, the proposed method did not generate a single false alarm. However, the average detection time is 1309 and 159 samples for $B = 10$ and $B = 100$ CPM, respectively. Nonetheless, the actual detection times have a high variation as shown in Figure 11(b).

It is instructive to compare our method with existing approaches:

- (a) Compared with the existing detection methods, our method has a more focused goal of detecting the point source rather than a general increase in measurement numbers. The SPRT in Step (ii) guarantees that it is uniformly the most powerful test at a given false alarm rate, in terms of maximizing the detection rate and minimizing the detection time.

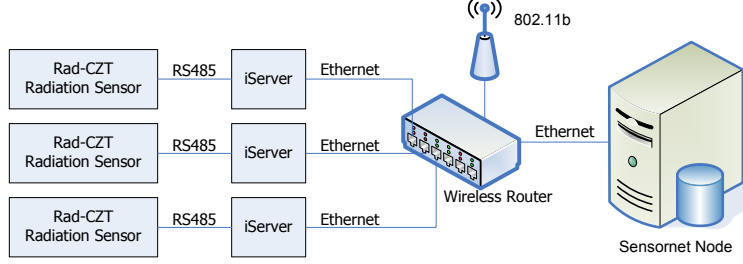
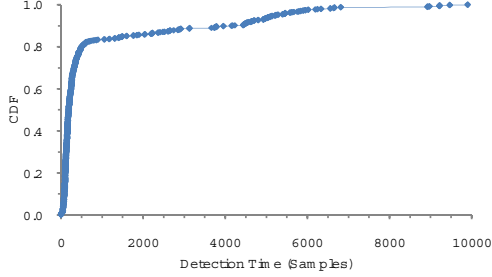
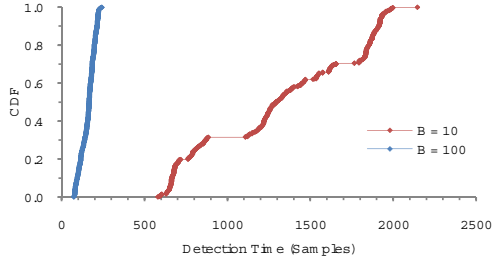


Fig. 12. Equipment setup in the radiation test-bed.



(a) Radiation source with rate $A_u = 10^6$ CPM and background with rate $B = 10$ CPM.



(b) No radiation source and background rate $B = 10$, and 100 CPM.

Fig. 11. Detection times for the source and background radiation.

- (b) Compared with the existing estimation methods, the ghost source phenomenon is strictly controlled by the false alarm probability in our method. Furthermore, the in-situ estimation of background radiation levels makes it sensitive to variations in the background radiation across the deployment area.
- (c) Compared with existing methods that utilize a detection method followed by estimation, the proposed method achieves a lower false alarm rate since the SPRT in Step (ii) does not have to account for all the possible source levels, but just the estimated one.

VII. EXPERIMENTAL TEST-BED RESULTS

A. Test-bed System Setup

We have set up three radiation detection test-beds at (1) the SensorNet Laboratory at Oak Ridge National

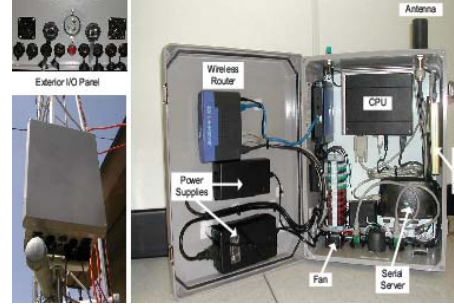


Fig. 13. The SensorNet node hardware.

Laboratory (ORNL), (2) Purdue University, and (3) University of Illinois at Urbana-Champaign. All three testbeds have similar configurations. Figure 12 shows the equipment layout of the test-bed for the experiments and Figure 20 shows the test-bed setup at ORNL. The test-bed at ORNL emulates the outdoor environment of courtyard shown in Figure 21. The components of the test-bed include a collection of Rad-CZT radiation sensors (currently 3 sensors) from RFTrax Inc. [1], a SensorNet node, and a wireless router.

For the experiments, the SensorNet node software is configured to poll each sensor every 4 seconds and store the sensor readings in a MySQL database. Due to limited storage on the SensorNet node, the database is configured to store only the 10,000 most recent samples of data. In addition to storing the sensor readings, we have augmented the SensorNet node software to send the sensor data to a workstation in real time for on-line analysis.

B. The SensorNet Node

The SensorNet node (see Figure 13) is a rugged hardware platform developed at ORNL with the goal of allowing a wide variety of sensors to be monitored and managed over a nation-wide distributed network. The wireless router allows the SensorNet nodes to communicate with each other as well as with an Ethernet switch connecting the sensors. The radiation sensors (RS485 devices) connect to the SensorNet node via iServer [2].

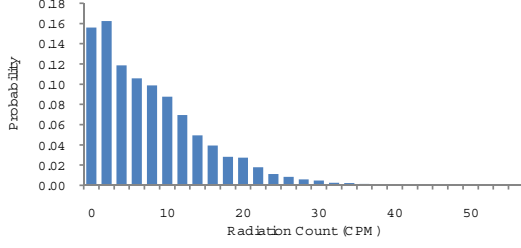


Fig. 14. Background radiation distribution in ORNL SensorNet Laboratory.

The iServer proxies the RS485/232 interface (for the radiation sensors in this case) to an Ethernet interface, thus providing access to the sensors via TCP/IP. In some configurations, the SensorNet node may be furnished with a broadband modem for connectivity over a cellular network. This may serve as a backup link if the primary connection over Ethernet/802.11 fails.

The Sensornet node runs the standard Linux operating system (Fedora Core) and a software package (the *node software*) developed by ORNL. The node software consists of a set of daemons that, under steady-state conditions, will perform the following operations:

- Query the sensors connected to the SensorNet node for data, and populate the MySQL database with the data. In addition, the node software analyzes the data to determine if an alert event should be issued. It utilizes IEEE 1451 as a means to communicate with a wide variety of sensors/actuators. IEEE 1451 wrappers are implemented for legacy devices that do not support the standard. For modern sensors that talk IEEE 1451, plug-and-play operation can be supported.
- Listen to the control center for configuration commands—for instance, setting the sensor polling rate and alert rules.
- Update the current location information for mobile SensorNet nodes and sensors.
- Archive the sensor data to a control center when requested; e.g., for offline data analysis.

For communication with the control center, each SensorNet node has multiple network connections. The node software uses at least two independent means to communicate with the control center, of which one is assigned as the primary connection. If the primary connection fails, the data are automatically rerouted through the secondary connection. The connectivity management module (CMM) monitors the health of all the network links available. The CMM periodically checks the connectivity to the control center, and reconfigures the network interface if the control center is unreachable.

Day 1			
Sensor	Mean	Stdev	#Samples
RFTTrax1	7.80	7.12	9900
RFTTrax2	7.46	7.01	9900
RFTTrax3	8.08	7.46	9900

Day 2			
Sensor	Mean	Stdev	#Samples
RFTTrax1	7.62	7.13	9900
RFTTrax2	7.54	7.07	9900
RFTTrax3	8.00	7.30	9900

TABLE I
STATISTIC OF BACKGROUND RADIATION IN SENSORNET LAB.

C. Background Radiation Profile

The three radiation sensors at ORNL test-bed were activated to collect radiation readings on two different days. A total of 9,900 samples were collected at a rate of one sample every 4 seconds, for about 11 hours. Figure 14 reports the distribution of the background radiation. The statistics of the data collected are reported in Table I.

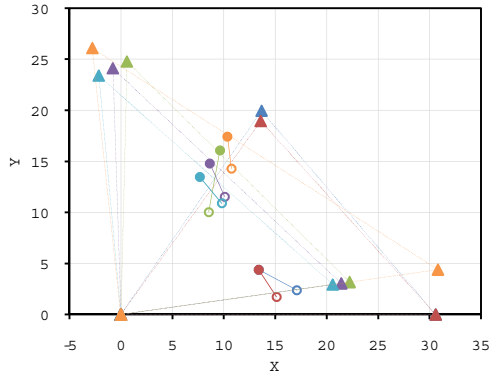
We performed the z-test for comparing the means of two independent samples to compare the radiation counts of the three sensors on the test-bed. The test results show that the probability of two sensors producing the same mean value is 0.63% at the maximum. In other words, the mean values are different with a 99.37% level of significance, even though the sensors are located within 2 feet of each other at the maximum. This experiment concludes that each sensor requires a separate background radiation profile.

D. Localization Method

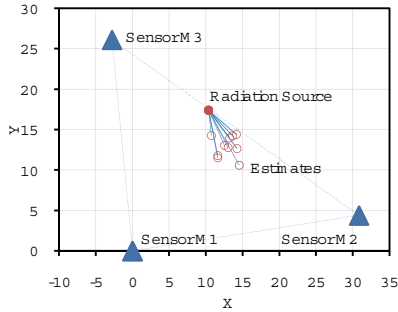
A Cs-137 radiation source of strength 0.95 μ -Curies was used on a table top with RFTTrax RAD-CZT sensors to collect measurements to estimate the locations of the source using the difference triangulation method described in Section IV-A. In each case, the number of measurements were within the range of [140, 170] samples. In Figure 15(a), we show example cases with different source locations and their estimates, and in Figure 15(b) we show repeated measurements with the same source and sensor locations. The performance of the localization method is summarized in Table II, wherein the top six rows correspond to different sensor and/or source locations and the other rows correspond to repeated measurements for the same sensor and source locations. The errors in the location estimates are plotted in Figure 16 with an average error of 4.87 inches. When no source is present, the localization method returns ghost sources, as shown in the two examples in Figure 17(a).

TABLE II
EXPERIMENTS WITH REAL RADIATION SOURCE (0.95μ CURIES)

Sensor M_1 (inches)	Sensor M_2 (inches)	Sensor M_3 (inches)	Radiation Source (X-Coord)	Radiation Source (Y-Coord)	Estimated Source (X-Coord)	Estimated Source (Y-Coord)	Error (inches)
(0.000, 0.000)	(30.602, 0.000)	(13.675, 19.949)	13.406	4.386	17.115	2.381	4.217
(0.000, 0.000)	(30.602, 0.000)	(13.594, 18.953)	13.406	4.386	15.136	1.739	3.163
(0.000, 0.000)	(22.247, 3.171)	(0.580, 24.782)	9.635	16.086	8.544	10.046	6.138
(0.000, 0.000)	(21.417, 3.053)	(-0.777, 24.123)	8.651	14.781	10.082	11.542	3.541
(0.000, 0.000)	(20.600, 2.937)	(-2.147, 23.407)	7.679	13.477	9.818	10.890	3.357
(0.000, 0.000)	(30.833, 4.395)	(-2.780, 26.101)	10.365	17.406	10.743	14.296	3.133
(0.000, 0.000)	(30.833, 4.395)	(-2.780, 26.101)	10.365	17.406	14.519	10.626	7.952
(0.000, 0.000)	(30.833, 4.395)	(-2.780, 26.101)	10.365	17.406	14.225	12.680	6.103
(0.000, 0.000)	(30.833, 4.395)	(-2.780, 26.101)	10.365	17.406	11.588	11.532	6.000
(0.000, 0.000)	(30.833, 4.395)	(-2.780, 26.101)	10.365	17.406	13.602	14.254	4.518
(0.000, 0.000)	(30.833, 4.395)	(-2.780, 26.101)	10.365	17.406	13.223	13.972	4.468
(0.000, 0.000)	(30.833, 4.395)	(-2.780, 26.101)	10.365	17.406	12.517	13.061	4.849
(0.000, 0.000)	(30.833, 4.395)	(-2.780, 26.101)	10.365	17.406	10.743	14.296	3.133
(0.000, 0.000)	(30.833, 4.395)	(-2.780, 26.101)	10.365	17.406	13.007	12.783	5.325
(0.000, 0.000)	(30.833, 4.395)	(-2.780, 26.101)	10.365	17.406	14.143	14.415	4.819
(0.000, 0.000)	(30.833, 4.395)	(-2.780, 26.101)	10.365	17.406	11.626	11.798	5.748



(a) Different sensor and source locations. The triangles denotes the sensors, filled circle denotes the actual location of radiation source, and non-filled circle denotes estimated location of the radiation source. Different color denotes a different measurement set.



(b) Different measurements with same source and sensor locations.

Fig. 15. Localization results of a Cs-137 radiation source.

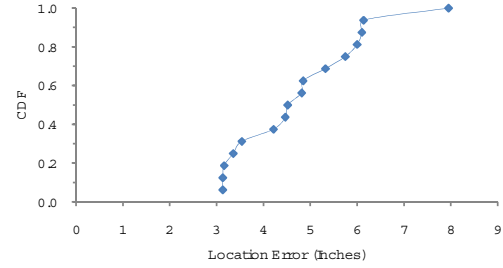
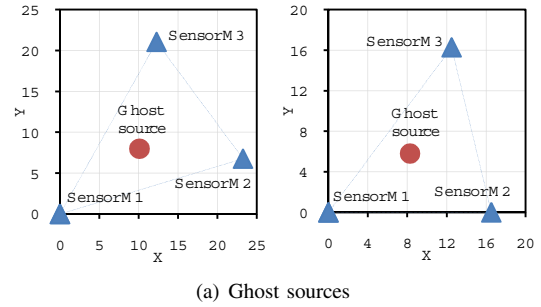
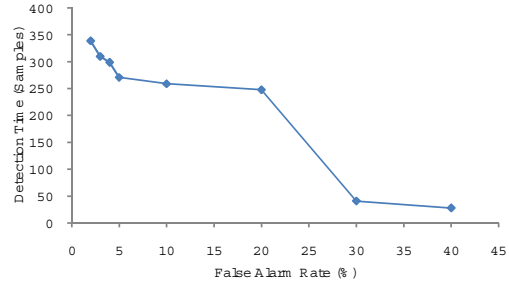


Fig. 16. Plot of location estimation errors corresponding to Table II.



(a) Ghost sources



(b) Detection time vs. false alarm rate.

Fig. 17. Ghost sources computed and rejected.

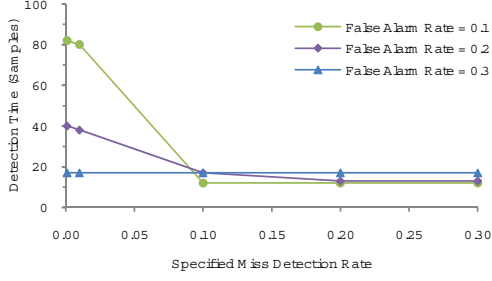


Fig. 18. Detection time is reduced as false alarm rate is increased.

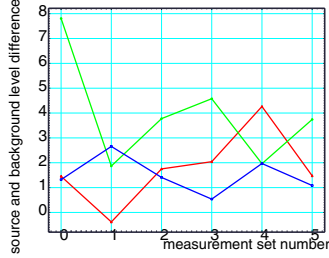


Fig. 19. Difference between average radiation levels with and without source present varies at each sensor across the measurement sets.

E. Identification Method

The identification method rejected the ghost sources computed based on the background readings shown in Figure 17 in both cases, but the decision time is a function of the false alarm rate $P_{1,0}$. When $P_{1,0} = 0.001$, the detection time was 339 samples but was reduced to 28 samples when the false alarm rate is increased from 2% to 40%, as shown in Figure 17(b).

The source detection rate varied based on τ , the number of initial measurements used before the SPRT was applied in the experiments. The radiation levels averaged over 10 minute intervals varied across the measurement sets both when a source is present and absent as indicated in Figure 19. For the case in Table II with $P_{0,1} = 0.1$, for $\tau \leq 10$, the empirical false alarm rate was 0.3, and was improved to 0.1 when $\tau = 25$, and reached 0.0 when $\tau = 75$. We next examine in detail the configuration that missed the detection for $\tau = 25$, corresponding to Row 5 in Table II, by varying $P_{0,1}$ in four repeated sets of measurements. The detection times are shown in Figure 18, which have lower values as we increase $P_{0,1} = 0.001, 0.01, 0.1, 0.2, 0.3$. Among the four sets of measurements, one set missed the detection of the source for $P_{1,0} = 0.1, 0.2, 0.3$.

F. Emulation of Larger Deployments and Stronger Sources

Our test-bed is implemented on a 100×100 square-inch workbench shown in Figure 20 using a radiation

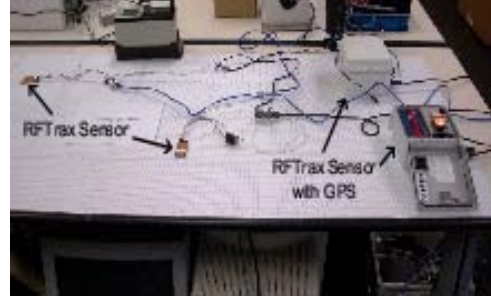


Fig. 20. Radiation detection workbench at ORNL.

point source of $0.95 \mu\text{-Curie}$. Larger monitoring areas such as the courtyard at ORNL shown in Figure 21 and stronger sources can be emulated using the test-bed as follows. Let r_{emulated} and r_{testbed} be the emulated distance and actual distance on the emulated monitoring area and workbench, respectively, such that $r_{\text{emulated}} = s_f \times r_{\text{testbed}}$. Sensor measurements of a radiation source of strength $A_{\text{testbed}}/r_{\text{testbed}}^2$ in the test-bed correspond to the measurements of a source of strength $A_{\text{emulated}} = s_f^2 A_{\text{testbed}}$ in the emulated area. For example, r_{emulated} is in meters for the courtyard shown in Figure 21 and r_{testbed} is in inches for the workbench. Then we have $s_f = 100 \text{ cm}/2.54 \text{ inch} = 39.37$, and thus, we can emulate a source with rate $A_{\text{emulated}} = 1549.99 \times A_{\text{testbed}}$ in the courtyard. The emulated source can have a strength of $1472 \mu\text{-Curies}$, which is much higher than the safe level. Thus, much stronger sources can be emulated, for the purpose of sensor measurements, in our test-bed using only much lower intensity sources, because the distances between the source and a sensor are also scaled. Hence, we are able to retain the complexity of the identification problem in the test-bed without using actual high intensity sources in the experiments. In particular, this emulation method can be used to map public open areas where radiation sources cannot be easily deployed. However, radiation sensors can be deployed in such areas to obtain background radiation measurements, which can then be used as measurements in the test-bed. This approach is somewhat limited when the background measurements are not the same in the emulated and workbench areas, but it would be more accurate than a simulation-only approach.

VIII. CONCLUSIONS

We have addressed the identification problem of a low-level point radiation source amidst background radiation. Our solution is achieved by a network of radiation sensors working in a tightly coupled two-step procedure. Based on measurements from the three sensors, the geometric difference triangulation method is used



Fig. 21. Emulated courtyard at ORNL.

to estimate the location and strength of the source. Then, a sequential probability ratio test based on current measurements and estimated parameters is employed to finally decide: (1) the presence of a source with the estimated parameters, or (2) the absence of the source, or (3) the insufficiency of measurements to make a decision. This method achieves the specified levels of the false alarm and missed detection probabilities, while ensuring a close-to-minimum number of measurements for reaching a decision. The proposed method mitigates the ghost-source problem of current estimation methods within a specified false alarm rate. It also achieves a lower false alarm rate compared with current detection methods by utilizing the estimated source parameters. We have tested and demonstrated our method using a test-bed that utilizes the scaling properties of point radiation sources to emulate high intensity sources that cannot be easily handled in practice due to safety and cost constraints.

There are several potential directions for future research. First, the localization method can be extended to 3D and to networks with more than three sensors to achieve increased robustness against environment and measurement uncertainties. Second, a more extensive experimental validation would be useful by using sources of multiple strengths. Third, the estimation of the source strength can be improved by using a training step wherein the fuser can be calibrated, for example, by determining both an offset and scale factors of the linear fuser.

ACKNOWLEDGMENTS

This work is funded by the SensorNet program at Oak Ridge National Laboratory which is managed by UT-Battelle, LLC for U.S. Department of Energy under Contract No. DE-AC05-00OR22725.

REFERENCES

- [1] <http://www.rftrax.com/radczt.html>.
- [2] <http://www.newportus.com/Products/ProdFam/iServer.htm>.
- [3] D. N. Anderson, D. C. Stromswold, S. C. Wunschel, A. J. Peurrung, and R. R. Hansen. Detection and location of Gamma-Ray sources with a modulating coded mask. *Technometrics*, 48(2):252–261, 2006.
- [4] Daniel E. Archer, Brock R. Beauchamp, G. Joseph Mauger, Karl E. Nelson, Michael B. Mercer, David C. Pletcher, Vincent J. Riot, James L. Schek, and David A. Knapp. Adaptable radiation monitoring system and method, 2006. U.S. Patent 7,064,336 B2.
- [5] Y. Bar-Shalom and X. R. Li. *Multitarget-Multisensor Tracking: Principles and Techniques*. YBS Publishing, 1995.
- [6] S. Blackman and R. Popoli. *Design and Analysis of Modern Tracking Systems*. Artech House, Boston, 1999.
- [7] S. M. Brennan, A. M. Mielke, and D. C. Torney. Radiation detection with distributed sensor networks. *IEEE Computer*, pages 57–59, August 2004.
- [8] P. E. Fehlau. Comparing a recursive digital filter with the moving-average and sequential probability-ratio detection methods for SNM portal monitors. *IEEE Transactions on Nuclear Science*, 40(2):143–146, 1993.
- [9] P. E. Fehlau. Comparing a recursive digital filter with the moving-average and sequential probability-ratio detection methods for SNM portal monitors. *IEEE Transactions on Nuclear Science*, 40(2):143–146, 1993.
- [10] A. Gunatilaka, B. Ristic, and R. Gailis. On localisation of a radiological point source. In *International Conference on Information, Decision and Control*. 2007.
- [11] J. W. Howse, L. O. Ticknor, and K. R. Muske. Least squares estimation techniques for position tracking of radioactive sources. *Automatica*, 37:1727–1737, 2001.
- [12] K. D. Jarman, L. E. Smith, and D. K. Carlson. Sequential probability ratio test for long-term radiation monitoring. *IEEE Transactions on Nuclear Science*, 51(4):1662–1666, 2004.
- [13] N. L. Johnson. Sequential analysis: A survey. *Journal of Royal Statistical Society, Series A*, 124(3):372–411, 1961.
- [14] G. F. Knoll. *Radiation Detection and Measurement*. John Wiley, 2000.
- [15] A. Mielke, D. Jackson, S. M. Brennan, M. C. Smith, D. C. Torney, A. B. Maccabe, and J.F. Karlin. Radiation detection with distributed sensor networks. In *SPIE Defense and Security Proceedings*, 2005.
- [16] D. Mihalas and B. W. Mihalas. *Foundations of Radiation Hydrodynamics*. Courier Dover Publications, 2000.
- [17] M. Morelande, B. Ristic, and A. Gunatilaka. Detection and parameter estimation of multiple radioactive sources. In *International Conference on Information Fusion*. 2007.
- [18] Karl E. Nelson, John D. Valentine, and Brock R. Beauchamp. Radiation detection method and system using the sequential probability ratio test, 2007. U.S. Patent 7,244,930 B2.
- [19] R. J. Nemzek, J. S. Dreicer, D. C. Torney, and T. T. Warnock. Distributed sensor networks for detection of mobile radioactive sources. *IEEE Transactions on Nuclear Science*, 51(4):1693–1700, 2004.
- [20] W. H. Press, S. A. Teukolsky, W. T. Vetterling, and B. P. Flannery. *Numerical Recipes in C*. Cambridge University Press, 1992.
- [21] N. S. V. Rao, X. Xu, and S. Sahni. A computational geometric method for dtoa triangulation. In *International Conference on Information Fusion*, 2007.
- [22] D. L. Stephens and A. J. Peurrung. Detection of moving radioactive sources using sensor networks. *IEEE Transactions on Nuclear Science*, 51(5):2273–2278, 2004.
- [23] A. Sundaresan, P. K. Varshney, and N. S. V. Rao. Distributed detection of a nuclear radioactive source using fusion of correlated decisions. In *International Conference on Information Fusion*, 2007.
- [24] H. L. Van Trees. *Detection, Estimation and Modulation Theory, Part I*. John Wiley, 1968.
- [25] P. K. Varshney. *Distributed Detection and Data Fusion*. Springer-Verlag, 1997.
- [26] G. B. Wetherill. *Sequential Methods in Statistics*. Methuen and Co., 1966.
- [27] X. Xu, N. S. V. Rao, and S. Sahni. A computational geometry method for localization using difference of distances. *ACM Transactions on Sensor Networks*, 2008. to appear.